This document is the accepted manuscript version of the following article:
Rosa, D. I. H., Hartloper, A., de Castro e Sousa, A., Lignos, D. G., Motavalli, M., & Ghafoori, E. (2021). Experimental behavior of iron-based shape memory alloys under cyclic loading histories. Construction and Building Materials, 272, 121712 (14 pp.). https://doi.org/10.1016/j.conbuildmat.2020.121712

This manuscript version is made available under the CC-BY-NC-ND 4.0 license http://creativecommons.org/licenses/by-nc-nd/4.0/

Experimental Behavior of Iron-based Shape Memory Alloys under Cyclic Loading Histories

Diego Isidoro Heredia Rosa[1], Alexander Hartloper[1], Albano de Castro e Sousa[1], Dimitrios G. Lignos[1,*], Masoud Motavalli[2], Elyas Ghafoori[2]

Abstract

The present paper investigates the behavior of iron-based shape memory alloys (Fe-SMAs) subjected to cyclic inelastic straining by means of uniaxial coupon experiments. The tests feature round bar coupons subjected to a broad range of uniaxial cyclic strain histories representative of earthquake loading. The experimental results suggest that the Fe-SMA under investigation exhibits an asymmetric stress-strain relation, with limited superelastic behavior. It was found that the post-yield/phase transformation behavior of the Fe-SMA alloy is both strain-rate and temperature-dependent. Quantitative comparisons with structural steels subjected to nominally identical cyclic strain histories indicate that, although the studied Fe-SMA has a similar energy dissipation per loading excursion with respect to conventional S355J2+N, the Fe-SMA's hardening response is appreciably higher, leading to comparatively larger elastic strain energies being stored.

Keywords: Iron-based shape memory alloys, Inelastic cyclic loading, Temperature dependency, Earthquake loading, Superelasticity, Smart materials

*Corresponding author: dimitrios.lignos@epfl.ch

[1]École Polytechnique Fédérale de Lausanne (EPFL), Station 18, 1015 Lausanne, Switzerland

[2]Swiss Federal Laboratories for Material Science and Technology (Empa), Überlandstrasse 129, 8600 Dübendorf, Switzerland

1. Introduction

Shape memory alloys (SMAs) are advanced materials exhibiting superelastic behavior and shape memory effect (SME) under thermomechanical loading. These two properties are due to a reversible phase transformation between martensite and austenite. Prior studies in the context of earthquake engineering suggest that the superelastic behavior of Nickel-Titanium SMAs (NiTi-SMAs) is promising for providing both energy dissipation and re-centering capabilities [1]. Examples in large-scale civil engineering applications using NiTi-SMAs include self-centering buckling-restrained braces [2], dampers with self-centering capabilities [3], as well as self-centering beam-column connections [4]. An extensive summary on the wide use of SMAs in seismic and wind engineering with emphasis on buildings, bridges [5, 6, 7, 8] as well as coastal structures [9] can be found in literature. In prior work, the mechanical behavior of NiTi SMAs has been characterised under cyclic tension and torsion for potential use in seismic applications [10, 11]. The main aspects that were investigated were the re-centering and energy dissipation capabilities when considered as energy dissipation elements. Because these applications were limited to wires the uniaxial compressive stress-strain response was not characterized. Similarly, Padgett et al. [12] has proposed and validated experimentally an SMA restrainer cable for seismic risk mitigation of bridges. Fugazza et al. [13] further explored the mechanical properties of SMAs when employed in devices for vibration control of buildings along with uniaxial constitutive modelling for nonlinear response history analysis. In a recently published study, Vignoli et al. [14] explored the dynamics of seismically resistant structures equipped with SMA composites and demonstrated that they can be an effective alternative for seismic risk mitigation as opposed to other response modification devices

However, NiTi-SMAs are prohibitively expensive for widespread use in large-scale infrastructure projects. Alternatively, iron-based (Fe-)SMAs are increasingly being produced at a lower cost than Ni-Ti-SMAs.

To date, the mechanical behavior of a broad range of Fe-SMA alloys with different

chemical compositions has been explored. Our current paper focuses on a refined version of an Fe-SMA developed by Janke [15], with the composition Fe-17Mn-5Si-10Cr-4Ni-1(V,C) (ma,-%). This material has been, and is currently, used for the pre-stress strengthening of civil infrastructure, with notable emphasis on existing bridges [16, 17, 18]. A general review of Fe-SMA properties relevant for retrofitting existing infrastructure under long term loading is provided in Cladera et al. [19]. Markedly, Fe-SMAs exhibit a lower level of superelasticity compared to NiTi-SMAs, however, they still show an appreciable shape memory effect [19].

The austenite/martensite phase composition of Fe-SMAs, and its evolution under thermomechanical loading, is particularly relevant since it governs the superelastic and SME properties of the material. Lee et al. [20] studied the phase evolution under tensile thermomechanical loading representative of the one used to pre-stress reinforced concrete structural components suitable for bridge applications. Lee et al. [20] identified three distinct phases when the material is loaded under monotonic tensile loading: 1) γ'-austenite, 2) ε-martensite, and 3) α'-martensite. The α'-martensite is an irreversible martensite variant that cannot be transformed to austenite, thereby preventing the SME. Moreover, Lee et al. [20] established the bounds on the temperature and stress at which martensite-to-austenite (reverse) phase transformation may occur. The above studies reveal that the reverse transformation of the Fe-SMA can occur at room temperatures below tensile stress levels of around 100 MPa. The α'-martensite phase was shown to only appear at temperatures above 100 °C, and therefore it does not seem to influence the Fe-SMA's behavior at room-temperatures under monotonic tensile loading. However, there are no bounds identified or established in the case that the material experiences compressive stresses as may be expected in the dissipative elements of steel structures in seismic regions.

The general consensus from an extensive literature review on the material properties of Fe-SMAs is that there are currently no comprehensive studies to characterize their behavior under cyclic inelastic straining similar to that seen during earthquake loading. Typical mechanical properties of the Fe-SMA under study such as the yield stress, the

elastic modulus, the ultimate tensile stress, as well as some low-cycle fatigue response features, have been identified in prior works [21, 22, 23]. Notable in Ghafoori et al. [22] are experimental results that suggest that strain-rate effects are present in the Fe-SMA's behavior. Therein, an increase in yield stress of ≈33 MPa between a test carried out at ≈0.03 %/sec and a test carried out at ≈1.4 %/sec is reported. In another study, Hosseini et al. [23] found that the maximum tensile stress of the Fe-SMA strips was ≈1000 MPa and they could elongate up to ≈55 % prior to fracture. Furthermore, although Ghafoori et al. [24] have studied the elevated temperature behavior of Fe-SMA alloys (under a fire exposure) up to 1000 ° C, the self-heating capability of the alloy under different strain rates has not been studied so far.

Although the above findings are of intrinsic value, material properties have hitherto been assessed by imposed loading histories that are deemed to be inadequate for seismic loading. Tests to date have mainly focused on characterizing mechanical and SME behavior solely under monotonic tensile or cyclic tensile loading, underscoring a lack of knowledge of this Fe-SMA under compressive strain demands that are likely to occur during earthquake loading. Other overlooked factors include the influence of strain level, strain rate, and temperature dependency on the material's SME or superelasticity (when present) at loading rates representing earthquake loading. Here, typical testing strain rates are generally not consistent with those expected during an earthquake event [25].

On the demand side, uncertainties (often titled record-to-record variability) in the earthquake ground motion hazard, in terms of both amplitude and frequency content, typically cause variability in the response characteristics of new and existing structures. Consequently, demands on the material itself can be highly variable and a need exists to assess its response under distinct loading histories. Studies with the objective of characterizing steel material behavior for seismic applications have addressed the issue of uncertainty by defining uniaxial strain demand protocols derived from the response of moment frames to a rich set of ground motions [26]. The same approach is used herein in an effort to comprehend the material behavior under such loading conditions.

The objective of the present paper is to characterize the macroscopic behavior of the Fe-17Mn-5Si-10Cr-4Ni-1(V,C) (ma,- %) Fe-SMA subjected to uniaxial tensile and compressive inelastic straining consistent with demands induced by earthquake loading. This objective is achieved through uniaxial cyclic experiments conducted on round bar coupon specimens. The next part of the paper describes the testing procedures and test apparatus used to perform the experiments on Fe-SMAs. The second part presents the results of the experimental campaign conducted on the Fe-SMA specimens. The third part contrasts experimental findings with available data from Fe-SMA materials with nominally identical chemical compositions that have been reported in the literature, as well as with results from commonly used structural steels in earthquake and structural engineering.

2. Methodology

The methodology to characterize the hysteretic behavior of the Fe-SMA comprises of an experimental campaign based on the ASTM E8/E8M guidelines [27] adapted for cyclic loading. This section discusses the details of the test apparatus along with the basic geometries of the Fe-SMA specimens (see Section 2.1), the employed strain-based load protocols (see Section 2.2), as well as the key analysis metrics used in interpreting the results and their data processing (see Section 2.3).

2.1. Test specimens and experimental apparatus

The geometry of a typical test specimen is presented in Figure 1. Particularly, the specimens are smooth round bar coupons designed to delay buckling until high compressive strains (i.e., larger than 5 %). This is shown in Figure 2, where the specimen is at 5 % inelastic uniaxial compressive strain and there is no buckling. Referring to Figure 1, the unreduced diameter of the specimen is 12 mm (with M12 threading), and the diameter of the reduced section is 6 mm. The gauge length of the specimen is designed such that buckling is prevented under inelastic uniaxial compressive loading as discussed in detail in de Castro e Sousa et al. [28]. To ensure the reliability of local

strain measurements with the 8 mm gauge length extensometer, we verified the same measurements with a video-extensometer that was used in preliminary verification testing of the overall test apparatus. The specimens are manufactured from coiled Fe-SMA reinforcing bars (rebars). To produce the specimens, the rebar coils are straightened, then the round bar coupons are machined according to the specifications in Figure 1.

The tests are conducted using a Schenk self-reacting frame available at EPFL Structural Laboratory (GIS), shown in Figure 3a, where the cross-beam is controlled by an electric actuator. A cross-section and plan-view of the test apparatus (Figures 4a and 4b, respectively) aid to explain the mounting process of a test specimen. In brief, the upper and lower adapter plates are bolted and prestressed to the upper cross-beam and the base, respectively. The three-piece outer ring, shown in Figure 4b, enables tensile loading of the specimen, while compressive loads are transferred directly from the counter nut to the lower plate. Importantly, the straightness of the mounted specimen is ensured by the straightness of the specimen itself and the perpendicularity of the machined threaded hole of the top plate. The lower plate is adjusted until the lower counter nut on the specimen enters its socket and is in contact with the plate. The nut and counter are then tightened against each other. Afterwards, the lower plate is bolted and pre-stressed to mobilize friction. The socket also provides lateral support, so that lateral forces can be absorbed by the lower plate and transferred to the reacting frame.

Figure 3b shows the test apparatus with a specimen installed in place along with the measurement devices. In particular, local strain measurements are obtained using an MTS extensometer with an 8 mm gauge length, force measurements are taken directly from the load cell attached to the top cross-beam of the Schenk frame, and the cross-beam displacement is recorded with a linear potentiometer. The surface temperature of a test specimen is recorded using a PT100 temperature sensor. Two cameras (shown in Figure 3a) are used to record videos at 60 frames per second in order to visually detect buckling of the specimen under compressive loading. This measure is put in place since visually detectable buckling deformations are perceptible

much sooner than degradation in the load-displacement curve. Only results prior to specimen buckling are considered to be meaningful at the material scale. Otherwise, the geometric nonlinearities are conflated with the sole material response.

The tests are controlled using a Proportional-Integral-Derivative (PID) algorithm with a Walter+Bai PCS8000 controller. All tests are conducted in load control up to $0.65f_y$, where f_y denotes the nominal yield stress of the Fe-SMA assumed to be $\approx$450 MPa [22]. The test execution is then switched to strain control using the MTS extensometer. Strain control allows for precise control over the desired strain rate depending on the load protocol of interest. Portions of the tests past 12.5 % strain are controlled using the cross-beam displacement due to the limit of the MTS extensometer. Stable control of the test becomes a critical issue when high strain rates are used, i.e., when $\dot{\varepsilon} \geqslant 1$ %/sec. For this reason, the value of the proportional gain is reduced from P (the best-fit gain calibrated to a square waveform) to $\tilde{P} = 1/3P$ to compensate the decrease in the tangent modulus of the specimen. The integral parameter (I) is left the same and the derivative (D) is set to zero (no compensation from the time change of the signal). It was found that this approximation allows for stable control of the testing machine at strain rates up to 8 %/sec.

2.2. Load protocols

The load protocols (LPs) comprise uniaxial strain histories applied to the Fe-SMA coupons. These are based on prior work by Suzuki [26], de Castro e Sousa et al. [28]. In brief, these protocols have been established based on nonlinear response history analyses of steel moment resisting frames featuring columns made of conventional or high performance steel. The suite of LPs features: a uniaxial monotonic test (LP1); two tests (LP2, LP3) representing different ground motion frequency characteristics followed by a large monotonic tensile push till specimen fracture; two constant amplitude tests (LP4, LP5) representative of long-duration ground motions that cycle a structure symmetrically at modest inelastic lateral drift demands (i.e., mean effects tend to be zero); three incremental tests (LP6, LP7, LP8) representative of ordinary earthquake

records scaled at design basis seismic intensities (i.e., 10 % probability of exceedance over 50 years) that cycle a structure symmetrically; and a test termed "random" (LP9) that is representative of ordinary, far-field and near fault ground motions scaled at a seismic intensity associated with a probability of exceedance of 2 % in 50 years.

The selected strain rates used in all the aforementioned protocols are informed by international material testing standards [27, 29]. The strain rate of 0.03 %/sec is selected for strain demands less than 2 % to load the specimens quasi-statically prior-to, and during, initial yielding, whereas the rate of 0.8 %/sec is selected for strain demands past this point.

The 2 % constant strain amplitude test (LP5) is chosen to study strain rate effects on the Fe-SMA's hysteretic behavior. Particularly, we conduct tests with the two standard strain rates (0.03 %/sec and 0.8 %/sec), complemented by a test at the rate of 8 %/sec. While the former rates are representative of quasi-static loading, the later approximates typical expected strain rates in steel structures during seismic events [25]. All tests are carried out at a room temperature of around 22 °C. Consistency of the experimental results between specimens subjected to LP5 is evaluated by conducting two additional tests per strain rate. Vis-a-vis the above discussion, the experimental program comprises 14 specimens in total.

In brief, the following tests are conducted:

- LP1: consists of monotonic tensile excursion until specimen fracture,
- LP2: consists of one cycle at 1 % strain amplitude in tension and compression, followed by a tensile excursion until specimen fracture,
- LP3: consists of one cycle at 4% strain amplitude in tension and compression, followed by a tensile excursion until specimen fracture,
- LP4: consists of 50 cycles with a constant strain of 1 % in tension and compression, with a strain rate of 0.03 %/sec,

- LP5_SR: consists of 50 cycles with a constant strain of 2 % in tension and compression, with a strain rate of 0.03 %/sec,

- LP5_MR: consists of 50 cycles with a constant strain of 2 % in tension and compression, with a strain rate of 0.8 %/sec,

- LP5_FR: consists of 10 cycles with a constant strain of 2 % in tension and compression, with a strain rate of 8 %/sec to ensure stability of the test for high strain rates. The specimen is then left for 5 minutes to cool down. In turn, 50 more loading cycles are imposed with identical strain amplitude and rate. Therefore, a total of 60 cycles was performed for LP5_FR,

- LP6: consists of incrementally increasing strain amplitude of 0.5 % until 8 % strain with a strain rate of 0.03 %/sec until 2 % strain and 0.8 %/sec after,

- LP7: consists of incrementally increasing strain amplitude of 1 % until 8 % strain with a strain rate of 0.03 %/sec until 2 % strain and 0.8 %/sec after,

- LP8: consists of incrementally increasing strain amplitude of 2 % until 8 % strain with a strain rate of 0.03 %/sec until 2 % strain and 0.8 %/sec after,

- LP9: consists of a "random" strain amplitude protocol. Due to an error in the test control, LP9 used herein is different than the standard "random" protocol discussed in Suzuki [26] and de Castro e Sousa et al. [28].

Results past compressive strains concurrent with buckling are not considered to be meaningful in the context of the present study and they are disregarded. A temperature gauge was used in most of the tests to track the variations in temperature while loading excluding LP1 and LP6.

2.3. Key metrics and data processing

The macroscopic material behavior of the Fe-SMA determined in this paper is based on true stress-true strain values. Engineering strain is computed using Equation 1,

$$\varepsilon_{eng} = \frac{L - L_0}{L_0} \tag{1}$$

where $L - L_0$ is the displacement measured from the extensometer, and $L_0 = 8$ mm from the extensometer gauge length. True strain is then calculated using Equation 2,

$$\varepsilon = \ln\left(1 + \varepsilon_{eng}\right) \tag{2}$$

Engineering stress is computed using Equation 3,

$$\sigma_{eng} = \frac{F}{A_0} \tag{3}$$

where F is the force measured from the load cell of the test apparatus, and A_0 is the initial cross sectional area of a specimen, computed using a diameter as measured by a conventional caliper gauge. True stress is then calculated using Equation 4,

$$\sigma = \sigma_{eng}\left(1 + \varepsilon_{eng}\right) \tag{4}$$

When subjected to inelastic strains, Fe-SMAs can develop both plastic and transformation strains [19]. Only the total strain is measured in the experiments, therefore, it is not possible to differentiate between the plastic and transformation strains. Hence, the term compound strain, referring to the combination of plastic and transformation strain is introduced to describe the Fe-SMA material behavior.

The elastic modulus E is determined with a line of best fit adjusted to the true stress-true strain data up to a stress of 100 MPa in the first loading excursion. The 0.2 % offset yield stress $\sigma_{p,0.2\%}$ is calculated according to ASTM [27]. A 0.01 % offset yield stress $\sigma_{p,0.01\%}$ is obtained similarly to $\sigma_{p,0.2\%}$. The ultimate tensile stress is calculated for load protocols that include a monotonic tensile excursion up to specimen fracture. The extensometer was removed prior to specimen fracture (12.5 % strain is

approximately the gauge's limit) in the current experimental program and, therefore, the ultimate tensile stress, σ_u, is defined based on the engineering stress,

$$\sigma_u = \frac{F_{max}}{A_0} \tag{5}$$

where F_{max} is the maximum force measured by the load cell. With respect to 0.2 % offset yield stress, for the Fe-SMA we do not differentiate between plastic deformation and phase transformation mechanisms.

A normalized parameter h is introduced in order to assess the level of cyclic hardening in a constant amplitude test present in the material in a quantitative manner. In particular, Equation 6 introduces the variable h, which corresponds to $\Delta\sigma$, that is the increase in stress due to cyclic hardening, divided by the 0.2 % offset yield stress. The values of $\Delta\sigma$ are computed as the increase in maximum stress due to cyclic hardening between the first loading cycle and the last loading cycle in the same loading direction of the constant 2 % strain amplitude with the 0.03 %/sec strain rate load protocol (LP5_SR),

$$h = \frac{\Delta\sigma}{\sigma_{p,0.2\%}} \cdot 100 \quad [\%] \tag{6}$$

Furthermore, to determine the Fe-SMA's potential for energy dissipation through cyclic straining, the portion of the area under the stress-strain relationship corresponding to the compound strain is computed using two different imposed load histories. The 2 % constant strain amplitude and the 1 % incrementally increasing strain amplitude protocols are selected for this purpose. Equation 7 represents the dissipated energy normalized by the elastic strain energy calculated using the mean 0.2 % offset yield stress and mean elastic modulus.

$$E^d_{cum} = \frac{\int \sigma(\varepsilon - \frac{\sigma}{E})d\varepsilon}{\frac{1}{2}\frac{\sigma^2_{p,0.2\%}}{E}} \tag{7}$$

The trapezoidal integration rule is used to integrate Equation 7.

The engineering strain at fracture, ε_{frac}, is computed using the relation between the cross-head displacement and the engineering strain. The relation is the extrapolated

for strain amplitudes grater than 12.5 %, where the MTS extensometer was removed due to its limit. The reported values reported herein for the engineering strain at fracture should only be considered as indicative. The authors do not think that the employed approach that has been used in prior studies as well is rational to extract the engineering strains at fracture, thereby leading to large reported values.

3. Results and discussion

3.1. Mechanical properties

Mechanical properties pertinent to structural analysis and design are summarized herein. These properties include the elastic modulus, E, the offset yield stresses, $\sigma_{p,0.2\%}$ and $\sigma_{p,0.01\%}$, the ultimate stress, σ_u, and the engineering fracture strain ε_{frac}. The material's mechanical properties are calculated according to the methodology described in Section 2.3, results for each parameter of interest, including the mean and coefficient of variation (CoV) based on all tests, are summarized in Table 1. The average results are: $E = 184$ GPa (CoV = 5.11 %), $\sigma_{p,0.01\%} = 267$ MPa (CoV = 22.7 %), and $\sigma_{p,0.2\%} = 450$ MPa (CoV = 13.7 %), and $\sigma_u = 950$ MPa. The LP5 medium- and fast-rate results are not included in the calculation of the mean values because of difference in loading rates.

Table 2 compares the mean of some of the aforementioned material properties obtained from the experimental campaign with indicative values found in literature for nominally identical Fe-SMA alloys [21, 22, 23]. Referring to Table 2, the values obtained from the experimental campaign are within bounds established in prior studies, thereby indicating confidence in the alloy's reproducibility of mechanical properties. The same observation holds true for the mean fracture strain reported in Table 1. Referring to Table 1, the fracture strains associated with LP2 and LP3 are smaller than that of LP1 due to the cumulative damage effect from the inelastic cycle prior to the monotonic tensile excursion to fracture. Notably, regardless of the amplitude of the inelastic cycles between LP2 and LP3, the fracture strain is fairly consistent between these two tests.

The CoV values summarized in Table 1 suggest that the mechanical properties of the Fe-SMA exhibit appreciable variability. Particularly, the variations in the alloy's material properties are evident as the CoV for the 0.2 % offset yield stress is nearly 14 %. The fairly large CoV values for the 0.2 % offset yield stress of the Fe-SMA should be contrasted to the corresponding CoV values of mechanical properties of conventional construction steels. For instance, in S355J0 steel (i.e., nominal yield stress, $f_y = 355$ MPa) the CoV around the material's yield stress is around 7 % [30]. The variations in the Fe-SMA yield stress may have been caused by residual stresses imposed in the coupon specimens due to the straightening of the rebar coils.

3.2. True stress-strain hysteretic behavior

This section summarizes the key characteristics of the observed true stress-strain behavior of the tested Fe-SMA. Figures 5 to 13 illustrate the true stress-true strain and temperature-true strain relationships obtained from each one of the specimens. Referring to Figures 6 to 13, it can be seen that the tested Fe-SMA does not exhibit a superelastic behavior, as is discussed in [31].

The results indicate an asymmetric stress-strain relation of the Fe-SMA under cyclic tensile/compressive inelastic loading. This asymmetry is evident in Figures 8a to 13a (LP4, LP5_SR, LP5_MR, LP5_FR, LP6, LP7, LP8 and LP9). These figures suggest that for strain amplitudes less than approximately 3 %, there are three distinct tangent moduli when the specimen is loaded in compression, as defined in Figure 14a. In state 1, the material experiences tensile strains while under tension. During stage 2, the material experiences tensile strain demands while under compressive loading and in stage 3, the material experiences compressive strain demands while being under compressive loading.

The tangent moduli appear to be dependent the magnitude of accumulated compound strain. Referring to Figures 10 to 12a (LP6, LP7 and LP8), the three tangent moduli are present for the cycles up to 3 % strain amplitude, while they are not visible in loading cycles with strain amplitudes larger than 3 %. Furthermore, constant am-

plitude tests show that after a certain number of cycles this phenomenon is no longer present; *c.f.* Figure 14 and the differences between its first and 50th cycle.

A possible reason for the observed asymmetry in the stress-strain response of the material under uniaxial cyclic loading may be due to activation of the reverse transformation at room temperatures depending on the stress level when the material is loaded in uniaxial compression. This same asymmetry is also observed in NiTi SMA bars [32]. Liu et al. [32] conducted uniaxial tensile and compressive tests, as well as uniaxial tension/compression tests on NiTi bars. They noticed that the behavior of NiTi SMA was asymmetric between tensile and compressive loading. This asymmetry in the behaviour of NiTi SMA was related to different deformation mechanisms. The existence of the three aforementioned distinct tangent moduli requires further studies of the microstructural behavior under cyclic loading to comprehend its physical basis and potentially refine the material for potential future use in seismic applications.

3.3. Influence of strain rate and temperature

This section discusses the influence of strain rate and temperature on the observed material behavior. The influence of strain rate and temperature is particularly relevant for seismic loading, which involves high strain rates up to around 8 %/sec. Not only does the high strain rate itself influence material response, but it also provides a rapid increase in temperatures due to yielding/ phase transformation. Depending on the geometry of the component loading rate, it might not have adequate time to cool down thereby accumulating heat by increasingly high temperature levels.

There is a marginal influence of the strain rate on the true stress-strain behavior of the Fe-SMA material between rates of 0.03 to 0.8 %/sec. Referring to Figures 6a, 7a, 10, 11a, 12a and 13a (LP2, LP3, LP6, LP7, LP8 and LP9, respectively), there is only a 35 MPa increase in stress when the strain rate increases from 0.03 %/sec to 0.8 %/sec at a 2 % uniaxial strain amplitude. In all these tests, the temperature at the strain rate transition point (first excursion past 2 % strain amplitude) is around 24 °C and has not increased while there is an increase in stress. Notably, the influence

of the strain rate on the resultant stress in this case is similar to that seen in mild steels [25, 33], and has been previously reported for the Fe-SMA by Ghafoori et al. [22].

Figure 9 shows the influence of the strain rate on the temperature rise. The surface temperatures in Figures 9b–9f correspond to three different strain rates. Figure 9f shows that when a strain rate of 8 %/sec (i.e., real time) is employed, the temperature measured at the surface of the gauge length increases by approximately 75 °C, while Figure 9b shows that when LP5 is conducted with a strain rate of 0.03 %/sec, the temperature measured at the same location only increases by about 2 °C. In the former, the measured temperature increases because there is much less time for the heat to be dissipated through both conduction and convection throughout the loading history. This is an important observation since in dampers dissipating energy through material yielding (e.g. buckling-restrained braces [34, 35]) the yielding core is typically wrapped with a debonding material, which in turn is encased in mortar. Therefore, the heat transfer mechanism through conduction is expected to occur at slower rates. This issue should be carefully examined in future studies associated with the use of Fe-SMAs in yield devices.

The cyclic hardening/softening behavior of the studied Fe-SMA might be dependent on the strain rate and/or the temperature. Referring to Figures 9a, 9c and 9e, for both LP5_SR and LP5_MR, cyclic hardening in tension and compression can be observed. On the other hand, for LP5_FR, cyclic softening in tension and compression is observed in the material's response. Further experiments that isolate the effects of strain rate and temperature are required to determine the cause of the switch from cyclic hardening to cyclic softening behavior.

3.4. Comparison with structural steels

This section compares the measured material properties of the studied Fe-SMA with two other structural steels. Particularly, the S355J2+N steel (nominal yield stress, f_y = 355 MPa) and the S690QL high strength steel (nominal yield stress, f_y = 690 MPa). The former steel is typical in seismic design of conventional and high performance steel

structures in Europe [36], with an impact test of 27 Joules at -20 °C. The latter steel is a high-grade structural steel, which is heat treated through quenching and tempering to improve its brittle properties. This structural steel has a low notch toughness testing temperature (i.e., typically 27 Joules at -40 °C).

In order to compare the material properties of the Fe-SMA with structural steels, data for S355J2+N and S690QL steels are taken from Grigoriou and Lignos [37], Forni et al. [38], Ho et al. [39]. The specimens in Grigoriou and Lignos [37] were round bar coupons similar to the ones tested in the present study. The round bar coupons were extracted from 25 mm thick steel plates. Whereas, the specimens in Forni et al. [38], Ho et al. [39] were round bar coupons and standard rectangular tensile coupons, respectively. The yield stress and elastic modulus properties of S355J2+N and S690QL steels are calculated using the procedures outlined in Section 2.3 using the data from Grigoriou and Lignos [37], while the values for the corresponding fracture strains are taken as reported in literature [38, 39]. Forni et al. [38] determined the fracture strain of S355J2+N steel by performing a monotonic tensile test with a strain rate of 0.1 %/sec on a round bar coupon and computed the strain at fracture using Equation **??**. Ho et al. [39] determined the strain at fracture of S690QL steel using digital image correlation (DIC) measurements.

Note that in Grigoriou and Lignos [37], tests were controlled using the cross-head displacement. The strain rates at which the tests were conducted were between 0.01 %/sec and 0.06 %/sec. Therefore, the strain rates used in Grigoriou and Lignos [37] are similar to the slow strain rate (0.03 %/sec) used in the present paper. In Grigoriou and Lignos [37], the constant 2 % strain amplitude protocol comprised 21 cycles for the S355J2+N steel. Due to issues associated with the PID control, only three full cycles were performed for the S690QL steel. In principle, comparisons between the two structural steels and the Fe-SMA should have been established at the aforementioned cycles given that the Fe-SMA was subjected to 50 constant cycles, as discussed in Section 2.2. However, the difference in number of cycles is not relevant for the present research, as both materials reached saturation (i.e., there is a negligible increase in the

absolute maximum value of stress between subsequent cycles) at the end of each test.

Table 3 summarizes the mean material characteristics of the Fe-SMA, S355J2+N, and S690QL steels. The mean Fe-SMA elastic modulus, 184 GPa, is less than the one commonly used for structural steels (i.e., 200 GPa). Table 3 suggests that the Fe-SMA has a higher 0.2 % offset yield stress, higher ultimate tensile stress and lower engineering fracture strain than that of the S355J2+N steel. On the other hand, the Fe-SMA has a lower yield stress, lower ultimate tensile stress and lower engineering fracture strain than those measured for the S690QL steel.

Referring to LP1 (Figure 16a), at a strain amplitude of 12.5 %, the corresponding stress is $\sigma_{12.5\%,Fe-SMA} = 931$ MPa for the Fe-SMA, $\sigma_{12.5\%,S355} = 527$ MPa for S355J2+N steels, and $\sigma_{12.5\%,S690} = 872$ MPa for the S690QL steel. These results indicate that the post-yield hardening ratio of the Fe-SMA is larger than that of both the S355J2+N and S690QL steels. The values of the parameter h recorded in Table 3 suggest that the amount of cyclic hardening of the Fe-SMA is larger than that of the S690QL steel, and equivalent to that of the S355J2+N steel. This can also be seen by the corresponding comparisons in Figure 16. The amount of hardening in the Fe-SMA material deserves much attention in future developments of this alloy for potential use in seismic applications. The reason is that the amount of hardening within a dissipative fuse (e.g., yield segment or zone) should be controlled to prevent damage in non-dissipative structural elements during strong ground motion shaking [40].

Referring to Figures 15 and 16, and based on the procedure outlined in Section 2.3, the potential for energy dissipation through cyclic straining of the Fe-SMA is compared to that of S355J2+N and S690QL steels by comparing (a) the stress-strain relations and (b) an equivalent cumulative dissipated energy of the three materials at a given loading history, normalized by their elastic strain energy. Figures 15 and 16b suggest that at a given strain amplitude, all three materials have the ability to dissipate energy through yielding/phase-transformation. However, S690QL and Fe-SMAs have higher elastic strain energies compared to S355J2+N steel. One typical use of yield dampers in seismic resistant design would be to cap the developed inertial forces along the height

of a building during an earthquake at a desired level [41]. Therefore, the higher elastic strain energy of the S690QL and Fe-SMA compared to S355J2+N steel implies that the developed inertial forces along the height of a structure equipped with yield dampers may still be fairly high depending on the amount of the elastic strain energy of the yielding segment. High inertial forces lead to appreciable absolute floor acceleration demands during an earthquake that could potentially cause damage to acceleration-sensitive non-structural content [42, 43, 44, 45, 46].

Referring to Figures 16c and 16d, the normalized cumulative energy dissipation as a function of strain excursion (i.e., half load cycle) is compared for all three materials. In all three cases, the S355J2+N steel with a lower yield stress has a higher potential for normalized energy dissipation followed by the Fe-SMA and S690QL regardless of the imposed strain history (i.e., incremental and constant amplitude). This is because the S355J2+N has the lowest elastic strain energy amongst the three materials. This further supports why lower yield stress steels are preferred over higher strength alloys in buckling restrained braces [35]. Referring to Figure 16c, the normalized cumulative dissipated energy exponentially increases while the strain excursion increases for the incremental protocol (LP7). This is due to the fact that the material does not exhibit stress saturation when it is subjected to the incremental protocol. Whereas, during LP5 (see Figure 16d) the rate of energy dissipation seems to decrease after the first excursion since the stress in all three materials stabilizes under constant strain amplitude.

4. Summary and Conclusions

This paper discusses the characterization of an iron-based shape memory alloy (Fe-SMA), Fe-17Mn-5Si-10Cr-4Ni-1(V,C) (ma,-%), under inelastic cyclic tensile/compressive straining. The examined strain-based loading histories are analogous to those that a steel material experiences as part of a dissipative component within a structure under strong ground motion shaking. Besides the typical mechanical properties of the Fe-SMA, key material properties of interest involve the amount of hardening for a given

loading history, the hardening saturation rate, as well as the material dependency to the strain-rate and temperature.

With regards to the Fe-SMA's mechanical properties, the coefficient of variation for the 0.2 % proportional limit stress is around 15 %, thereby indicating an appreciable variability in the material properties between specimens. This is attributed to potential residual stresses due to straightening of the rebar coils prior to machining of the specimens.

The experimental results indicate an asymmetric stress-strain relation between tensile and compressive straining. This is observable fairly well on the constant amplitude cyclic tests. In particular, there are three distinct tangent moduli in the true stress-true strain relation when the specimen is loaded in compression but not in tension. The first one corresponds to the elastic modulus of the specimen, whereas the last two tangent moduli require microstructure analysis to comprehend their physical bases. Interestingly, the same moduli appear to be dependent on the accumulated compound strain.

Additionally, strain rates between 0.03 %/sec and 0.8 %/sec do not significantly influence the Fe-SMA's behavior. The surface temperature of the material within its gauge length also seems to be fairly stable for those strain rate ranges. However, that temperature increases when the imposed strain rate attains values similar to those expected during earthquake loading. For instance, for a given load protocol, an increase of 75 °C in temperature is observed at 8 %/sec, compared to 2 °C at 0.03 %/sec. The difference in surface temperature is attributed to a higher rate of heat generation than the rate of heat dissipation through conduction and convection for tests at higher strain rates. The observed temperature increase at strain rate loading equivalent to those observed in earthquake loading may influence the phase transformation of the Fe-SMA material. While stress-temperature phase diagrams of this material are only available for tensile loading [20], it is recommended that such diagrams should be derived for the above described loading conditions by means of future experimental studies.

The cyclic hardening/softening behavior of the studied Fe-SMA is dependent on

the strain rate and temperature. Particularly, an increase in stress of around 50 MPa due to cyclic hardening is observed in both tension and compression for the slow rate (0.03 %/sec) and the intermediate rate (0.8 %/sec) for the constant 2 % strain amplitude tests. Whereas cyclic softening of approximately 50 MPa can be observed in both tensile and compressive loading excursions for the same strain amplitude test carried out at a high strain rate (8 %/sec).

Direct comparisons with other commonly used structural steels (S355J2+N and S690QL) reveal that the 0.2 % proportional limit stress of the studied Fe-SMA is higher than the one of a S355J2+N steel, and lower than that of a S690QL steel. The strain at fracture of the studied Fe-SMA is also lower than the corresponding values for both the S355J2+N and S690QL steels. Referring to the constant 2 % strain amplitude with a 0.03 %/sec strain rate load protocol (LP5_SR), the amount of cyclic hardening of the Fe-SMA is larger by around 90 % than that of the S690QL steel and around 15 % smaller than that of the S355J2+N steel. Albeit the total energy dissipation per loading excursion (i.e., half-cycle) of the Fe-SMA is nearly the same with that of a S355J2+N steel, the potential of the latter in yield damper applications to reduce the absolute floor acceleration demands along a building's height is still larger than that of high-yield stress alloys (e.g., Fe-SMA and S690QL). The reason is that low yield stress steels do not have appreciable elastic strain energy.

5. Acknowledgments

The authors graciously thank re-fer AG to provide the Fe-SMA material used in this study. Additional funding for the financial support of the first, second and third authors was provided by EPFL. This support is gratefully acknowledged. The authors would also like to acknowledge the technical assistance of lab personnel (Mr. Gilles Guignet and Mr. Sylvain Demierre) within the Structures Laboratory (GIS) at EPFL for the execution of the experimental program and instrumentation discussed in this paper. Any opinions, findings, and conclusions or recommendations expressed in this paper are those of the authors and do not necessarily reflect the views of the sponsors.

References

[1] R. DesRoches, J. McCormick, M. Delemont, Cyclic Properties of Superelastic Shape Memory Alloy Wires and Bars, Journal of Structural Engineering 130 (2004) 38–46.

[2] D. J. Miller, L. A. Fahnestock, M. R. Eatherton, Development and experimental validation of a nickel–titanium shape memory alloy self-centering buckling-restrained brace, Engineering Structures 40 (2012) 288–298.

[3] H. Ma, C. Cho, Feasibility study on a superelastic SMA damper with re-centring capability, Materials Science and Engineering: A 473 (2008) 290–296.

[4] M. S. Speicher, R. DesRoches, R. T. Leon, Experimental results of a NiTi shape memory alloy (SMA)-based recentering beam-column connection, Engineering Structures 33 (2011) 2448–2457.

[5] J. C. Wilson, M. J. Wesolowsky, Shape Memory Alloys for Seismic Response Modification: A State-of-the-Art Review, Earthquake Spectra 21 (2005) 569–601.

[6] G. Song, N. Ma, H.-N. Li, Applications of shape memory alloys in civil structures, Engineering Structures 28 (2006) 1266–1274.

[7] J. Dong, C. S. Cai, A. M. Okeil, Overview of Potential and Existing Applications of Shape Memory Alloys in Bridges, Journal of Bridge Engineering 16 (2011) 305–315.

[8] K. C. Shrestha, M. S. Saiidi, C. A. Cruz, Advanced materials for control of post-earthquake damage in bridges, Smart Materials and Structures 24 (2015) 025035.

[9] S. Saadat, M. Noori, H. Davoodi, Z. Hou, Y. Suzuki, A. Masuda, Using NiTi SMA tendons for vibration control of coastal structures, Smart Materials and Structures 10 (2001) 695–704.

[10] M. Dolce, D. Cardone, Mechanical behaviour of shape memory alloys for seismic applications 1. Martensite and austenite NiTi bars subjected to torsion, International Journal of Mechanical Sciences 43 (2001) 2631–2656.

[11] M. Dolce, D. Cardone, Mechanical behaviour of shape memory alloys for seismic applications 2. Austenite NiTi wires subjected to tension, International Journal of Mechanical Sciences 43 (2001) 2657–2677.

[12] J. E. Padgett, R. DesRoches, R. Ehlinger, Experimental response modification of a four-span bridge retrofit with shape memory alloys, Structural Control and Health Monitoring 17 (2009) 694–708.

[13] D. Fugazza, F. Auricchio, D. A. Pavese, D. L. Petrini, Shape-Memory Alloy Devices in Earthquake Engineering: Mechanical Properties, Constitutive Modelling and Numerical Simulations, Ph.D. thesis, Università degli Studi di Pavia, Pavia, 2003.

[14] L. L. Vignoli, M. A. Savi, S. El-Borgi, Nonlinear dynamics of earthquake-resistant structures using shape memory alloy composites, Journal of Intelligent Material Systems and Structures 31 (2020) 771–787.

[15] L. Janke, Applications of shape memory alloys in civil engineering structures - Overview, limits and new ideas, Materials and Structures 38 (2005) 578–592.

[16] M. Izadi, E. Ghafoori, M. Shahverdi, M. Motavalli, S. Maalek, Development of an iron-based shape memory alloy (Fe-SMA) strengthening system for steel plates, Engineering Structures 174 (2018) 433–446.

[17] M. Izadi, A. Hosseini, J. Michels, M. Motavalli, E. Ghafoori, Thermally activated iron-based shape memory alloy for strengthening metallic girders, Thin-Walled Structures 141 (2019) 389–401.

[18] M. Izadi, M. Motavalli, E. Ghafoori, Iron-based shape memory alloy (Fe-SMA) for fatigue strengthening of cracked steel bridge connections, Construction and Building Materials 227 (2019) 116800.

[19] A. Cladera, B. Weber, C. Leinenbach, C. Czaderski, M. Shahverdi, M. Motavalli, Iron-based shape memory alloys for civil engineering structures: An overview, Construction and Building Materials 63 (2014) 281–293.

[20] W. Lee, B. Weber, G. Feltrin, C. Czaderski, M. Motavalli, C. Leinenbach, Phase transformation behavior under uniaxial deformation of an Fe–Mn–Si–Cr–Ni–VC shape memory alloy, Materials Science and Engineering: A 581 (2013) 1–7.

[21] M. Koster, W. Lee, M. Schwarzenberger, C. Leinenbach, Cyclic deformation and structural fatigue behavior of an FE–Mn–Si shape memory alloy, Materials Science and Engineering: A 637 (2015) 29–39.

[22] E. Ghafoori, E. Hosseini, C. Leinenbach, J. Michels, M. Motavalli, Fatigue behavior of a Fe-Mn-Si shape memory alloy used for prestressed strengthening, Materials & Design 133 (2017) 349–362.

[23] E. Hosseini, E. Ghafoori, C. Leinenbach, M. Motavalli, S. R. Holdsworth, Stress recovery and cyclic behaviour of an Fe–Mn–Si shape memory alloy after multiple thermal activation, Smart Materials and Structures 27 (2018) 025009.

[24] E. Ghafoori, M. Neuenschwander, M. Shahverdi, C. Czaderski, M. Fontana, Elevated temperature behavior of an iron-based shape memory alloy used for prestressed strengthening of civil structures, Construction and Building Materials 211 (2019) 437–452.

[25] C.-P. Lamarche, R. Tremblay, Seismically induced cyclic buckling of steel columns including residual-stress and strain-rate effects, Journal of Constructional Steel Research 67 (2011) 1401–1410.

[26] Y. Suzuki, Earthquake-induced collapse of steel moment resisting frames with conventional and high performance steel columns, Ph.D. thesis, McGill University, Montreal, Canada, 2018.

[27] ASTM, E8/E8M - 16a - Standard test methods for tension testing of metallic materials, West Conshohocken, PA, USA, 2016.

[28] A. de Castro e Sousa, Y. Suzuki, D. Lignos, Consistency in Solving the Inverse Problem of the Voce-Chaboche Constitutive Model for Plastic Straining, Journal of Engineering Mechanics 146 (2020) 04020097.

[29] CEN, EN 10002-1:2001 - Metallic materials Tensile testing Part 1: method of test at ambient temperature, European Committee for Standardization, Brussels, Belgium, 2001.

[30] A. Braconi, M. Finetto, H. Degee, N. Hausoul, B. Hoffmeister, M. Gündel, S. A. Karmanos, G. Varelis, R. Obiala, M. Hjaij, H. Somja, M. Badalassi, S. Caprili, W. Salvatore, P. Pappa, V. Rinaldi, European Commission, Directorate-General for Research and Innovation, Optimising the seismic performance of steel and steel-concrete structures by standardising material quality control (OPUS)., Publications Office, Luxembourg, 2013. OCLC: 870631851.

[31] C. Czaderski, B. Weber, M. Shahverdi, M. Motavalli, C. Leinenbach, W. Lee, R. Brönnimann, J. Michels, Iron-based shape memory alloys (Fe-SMA) - a new material for prestressing concrete structures, Proceedings of SMAR 2015 the 3rd conference on smart monitoring, assessment and rehabilitation of civil structures (2015) 12.

[32] Y. Liu, Z. Xie, J. Van Humbeeck, L. Delaey, Asymmetry of stress–strain curves under tension and compression for NiTi shape memory alloys, Acta Materialia 46 (1998) 4325–4338.

[33] M. Wakabayashi, T. Nakamura, S. Iwai, Y. Hayashi, Effects of strain rate on the behavior of structural members subjected to earthquake forces, 8th World Conference on Earthquake Engineering (1984).

[34] T. Yamaguchi, Y. Nakata, T. Takeuchi, T. Ikebe, T. Nagao, A. Minami, T. Suzuki, Seismic control devices using low-yield-point steel, Shinnittetsu Giho (1998).

[35] C. J. Black, N. Makris, I. D. Aiken, Component Testing, Seismic Evaluation and Characterization of Buckling-Restrained Braces, Journal of Structural Engineering 130 (2004) 880–894.

[36] CEN, Eurocode 8: Design of Structures for Earthquake Resistance - Part 1: General Rules, Seismic Actions and Rules for Buildings, European Committee for Standardization, Brussels, Belgium, 2004.

[37] V. Grigoriou, D. G. Lignos, Characterization of the cyclic hardening properties of european steels., (Unpublished report), EPFL, Lausanne, 2017.

[38] D. Forni, B. Chiaia, E. Cadoni, Strain rate behaviour in tension of S355 steel: Base for progressive collapse analysis, Engineering Structures 119 (2016) 164–173.

[39] H. Ho, K. Chung, X. Liu, M. Xiao, D. Nethercot, Modelling tensile tests on high strength S690 steel materials undergoing large deformations, Engineering Structures 192 (2019) 305–322.

[40] ANSI/AISC, ANSI/AISC 341-16: Seismic Provisions For Structural Steel Buildings, American Institute of Steel Construction, Chicago, Illinois, 2016.

[41] C. Christopoulos, A. Filiatrault, Principle of Passive Supplemental Damping and Seismic Isolation, IUSS Press, 2006.

[42] E. Reinoso, E. Miranda, Estimation of floor acceleration demands in high-rise buildings during earthquakes, The Structural Design of Tall and Special Buildings 14 (2005) 107–130.

[43] S. R. Uma, J. X. Zhao, A. B. King, Seismic actions on acceleration sensitive non-structural components in ductile frames, Bulletin of the New Zealand Society for Earthquake Engineering 43 (2010) 110–125.

[44] S.-H. Hwang, D. G. Lignos, Effect of Modeling Assumptions on the Earthquake-Induced Losses and Collapse Risk of Steel-Frame Buildings with Special Concentrically Braced Frames, Journal of Structural Engineering 143 (2017) 04017116.

[45] S.-H. Hwang, D. G. Lignos, Earthquake-induced loss assessment of steel frame buildings with special moment frames designed in highly seismic regions, Earthquake Engineering & Structural Dynamics 46 (2017) 2141–2162.

[46] E. Miranda, A. K. Kazantzi, D. Vamvatsikos, New Approach to the Design of Acceleration-sensitive Non-structural Elements in Buildings, in: 16th European Conference on Earthquake Engineering, Thessaloniki.

Table 1: Summary of mechanical properties for the Fe-17Mn-5Si-10Cr-4Ni-1(V,C) (ma,-%) alloy.
a: For the mean and CoV, the results of LP5_MR and LP5_FR are not taken into account.

LP	Spec.	E [GPa]	$\sigma_{p,0.01\%}$ [MPa]	$\sigma_{p,0.2\%}$ [MPa]	ε_{frac} [%]	σ_u [MPa]
LP1	1	163	373	534	54	946
LP2	1	187	282	472	48	953
LP3	1	178	263	454	44	952
LP4	1	189	209	442	-	-
LP5_SR	1	196	239	307	-	-
	2	183	358	519	-	-
LP5_MR	1	172	144	435	-	-
	2	187	125	308	-	-
LP5_FR	1	174	96	258	-	-
	2	176	158	467	-	-
LP6	1	178	239	438	-	-
LP7	1	193	178	419	-	-
LP8	1	188	277	469	-	-
LP9	1	187	248	450	-	-
Mean [a]		184	267	450	49	950
CoV [%] [a]		5.11	22.7	13.7	10.3	0.4

Table 2: Comparison of the mechanical properties for the Fe-17Mn-5Si-10Cr-4Ni-1(V,C) (ma,-%) alloy from the present study with reported values.

Reference	E [GPa]	$\sigma_{p,0.01\%}$ [MPa]	$\sigma_{p,0.2\%}$ [MPa]	ε_{frac} [%]	σ_u [MPa]
Koster et al. [21]	200	190	310	-	993
Ghafoori et al. [22]	173	230	546	55	1015
Hosseini et al. [23]	173	230	546	55	1015
Present Study	184	267	450	54	950

Table 3: Fe-17Mn-5Si-10Cr-4Ni-1(V,C) (ma,-%) Fe-SMA and structural steels properties.
a: steel data from [37] b: data from [38] c: data from [39].

Material	E [GPa]	$\sigma_{p,0.01\%}$ [MPa]	$\sigma_{p,0.2\%}$ [MPa]	ε_{frac} [%]	h [%]	σ_u [MPa]
S355J2+N [a]	200	375	362	27 [b]	13.3	553
S690QL [a]	200	614	714	15.5 [c]	4.37	1000
Fe-SMA	184	267	450	54	11.7	950

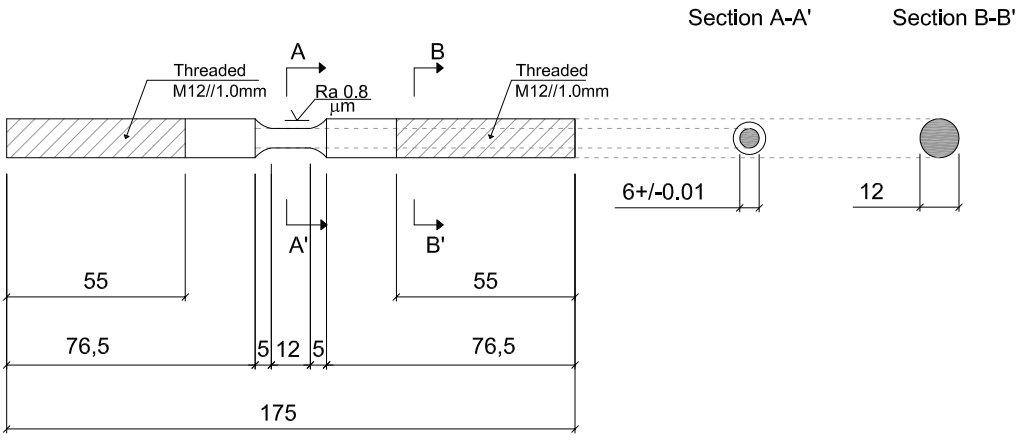

Figure 1: Geometry of the round-bar coupon specimens [mm]

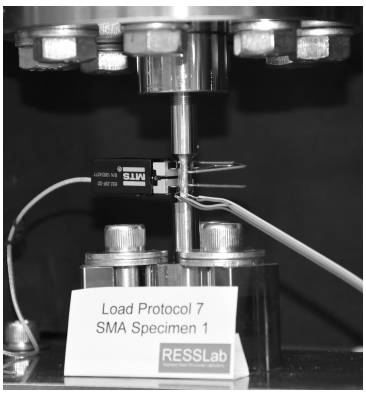

Figure 2: Specimen at 5 % inelastic uniaxial compressive strain

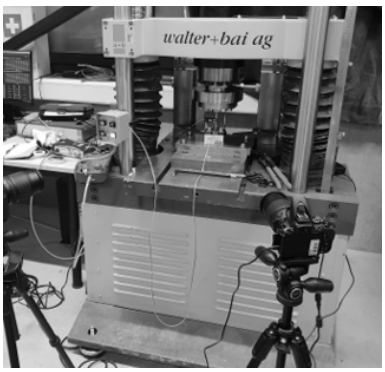

(a) Experimental setup

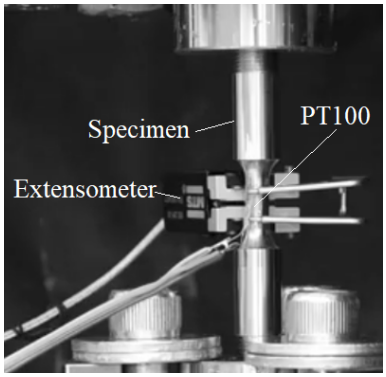

(b) Detailed view of the specimen

Figure 3: Test apparatus and detailed view of round bar coupon specimens

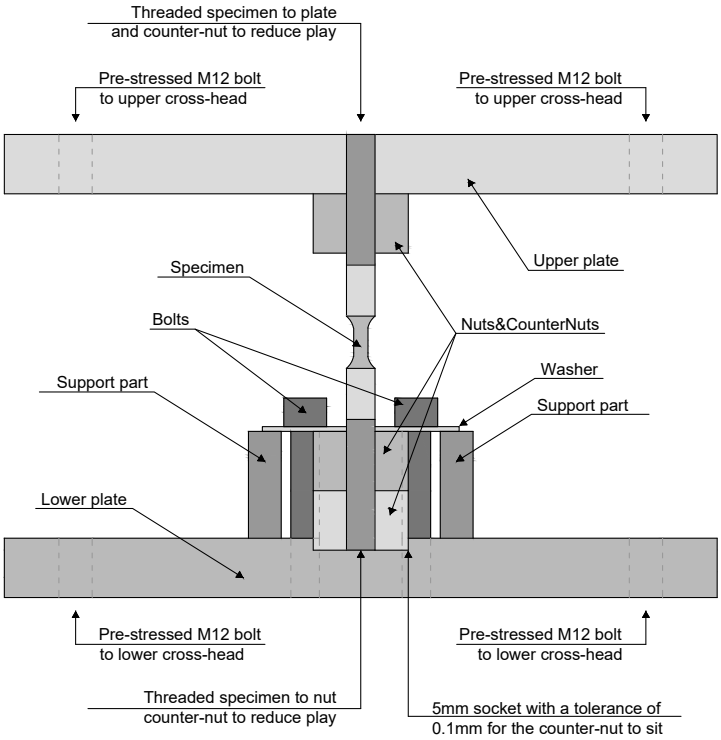

(a) Cross-section

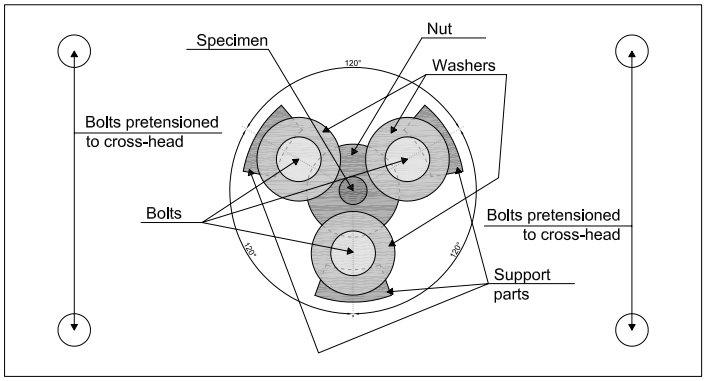

(b) Plan view

Figure 4: Cross-section and plan view of the uniaxial cyclic test setup

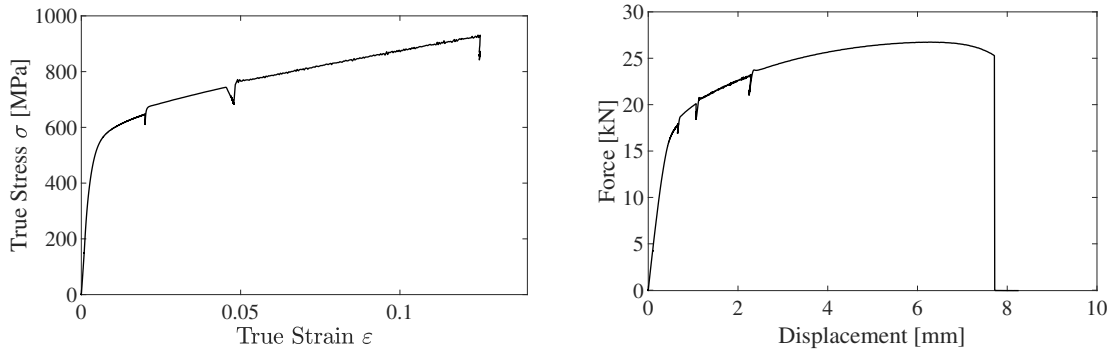

(a) True stress-true strain

(b) Force-displacement

Figure 5: Fe-SMA material behavior LP1 (0.03 %/sec up to 2 % strain amplitude and 0.8 %/sec after)

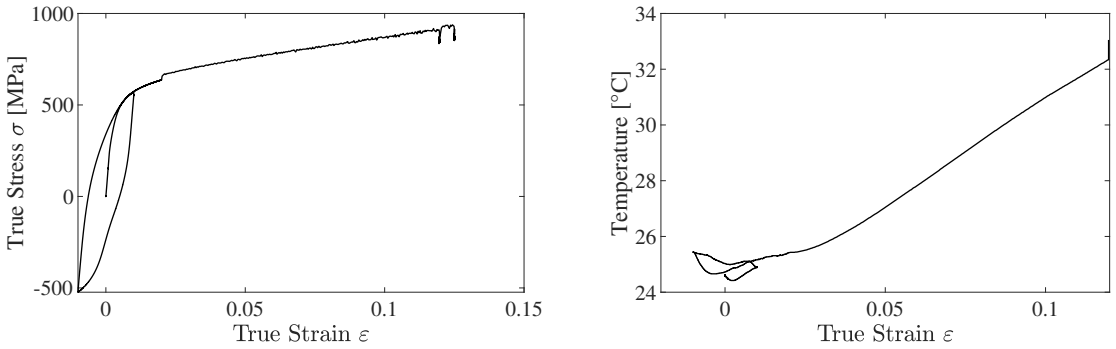

(a) True stress-true strain

(b) Temperature-true strain

Figure 6: Fe-SMA material behavior LP2 (0.03 %/sec up to 2 % strain amplitude and 0.8 %/sec after)

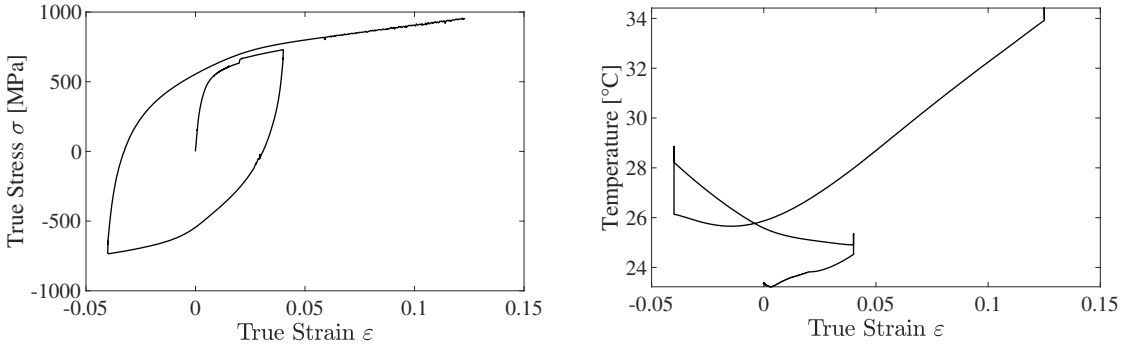

(a) True stress-true strain

(b) Temperature-true strain

Figure 7: Fe-SMA material behavior LP3 (0.03 %/sec up to 2 % strain amplitude and 0.8 %/sec after)

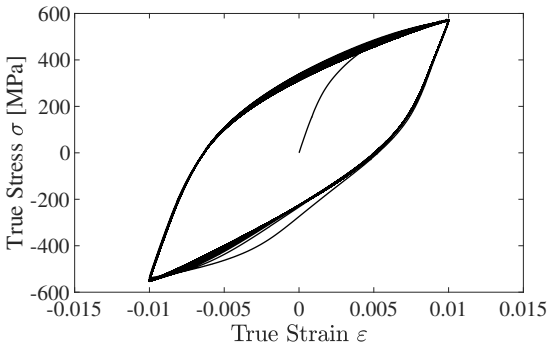

(a) True stress-true strain

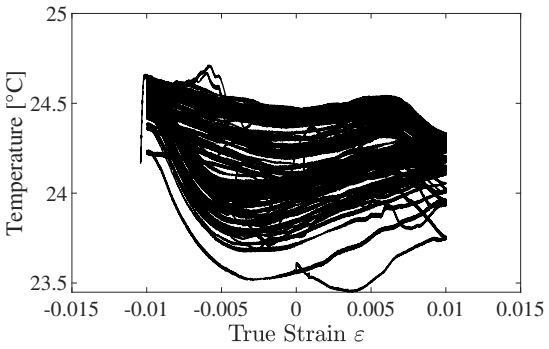

(b) Temperature-true strain

Figure 8: Fe-SMA material behavior LP4 (0.03 %/sec)

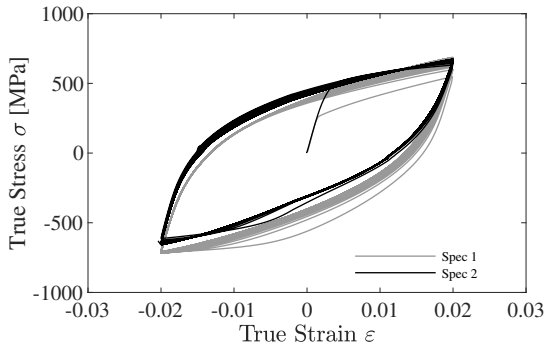

(a) True tress-true strain LP5_SR

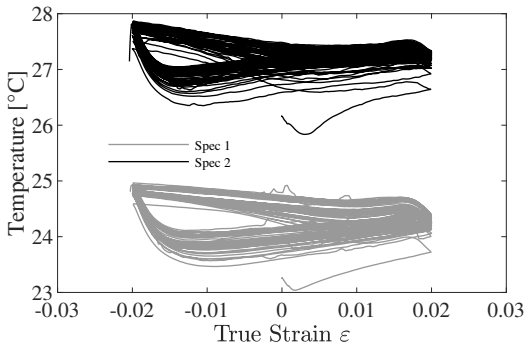

(b) Temperature-true strain LP5_SR

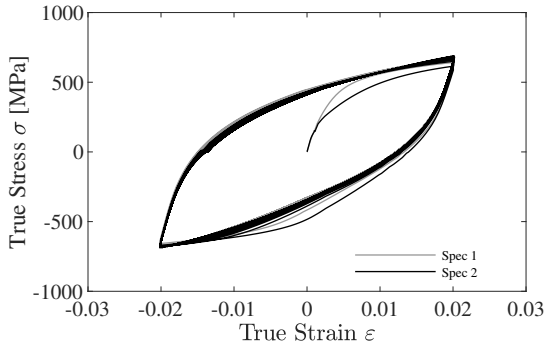

(c) True tress-true strain LP5_MR

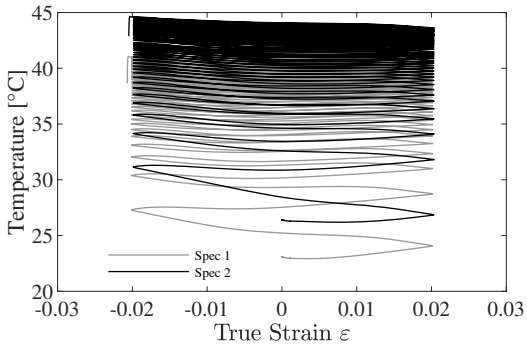

(d) Temperature-true strain LP5_MR

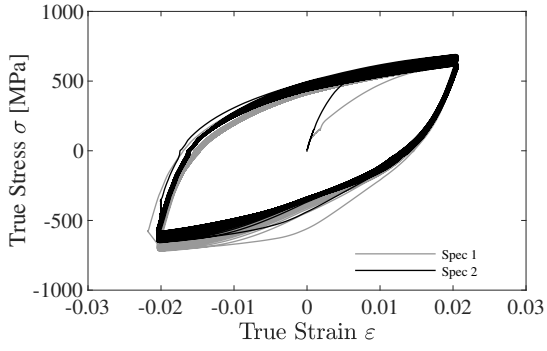

(e) True tress-true strain LP5_FR

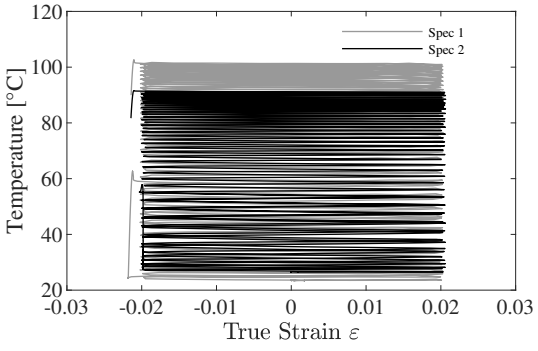

(f) Temperature-true strain LP5_FR

Figure 9: Fe-SMA material behavior LP5 - influence of strain rate on the true-stress-true strain and the temperature-true strain relationships

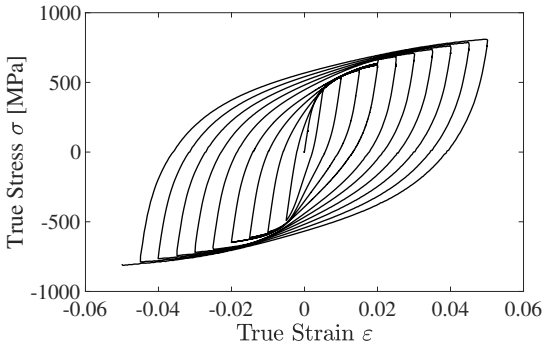

Figure 10: True stress-true strain LP6 (0.03 %/sec up to 2 % strain amplitude and 0.8 %/sec after)

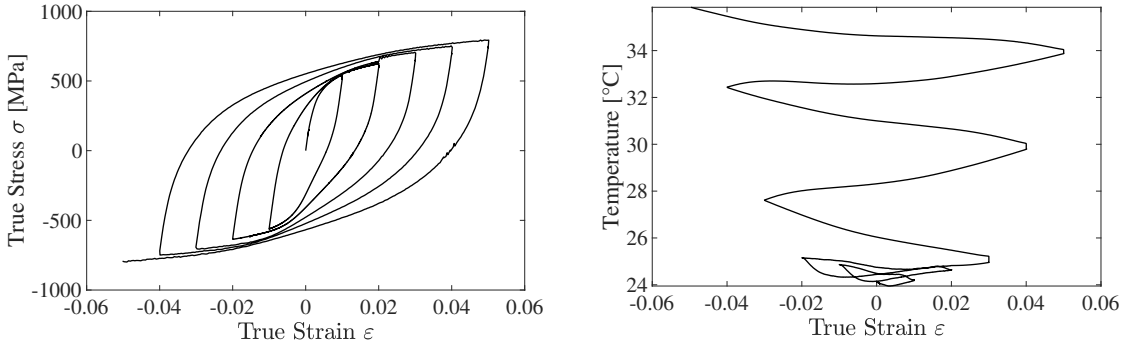

(a) True stress-true strain

(b) Temperature-true strain

Figure 11: Fe-SMA material behavior LP7 (0.03 %/sec up to 2 % strain amplitude and 0.8 %/sec after)

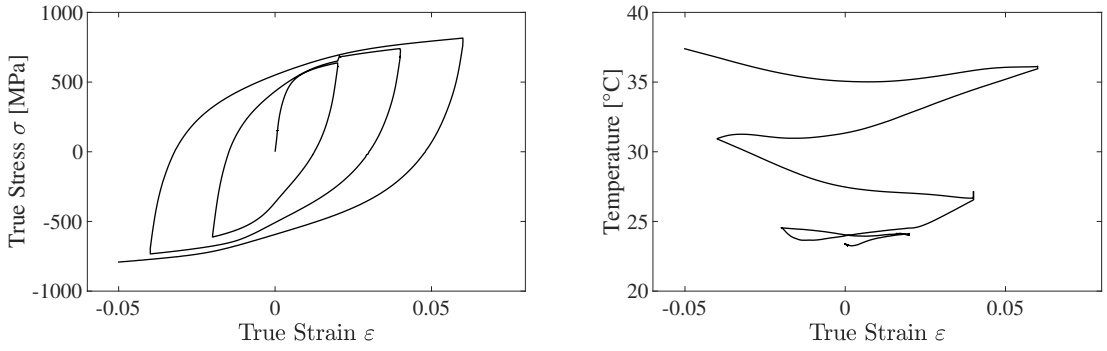

(a) True stress-true strain

(b) Temperature-true strain

Figure 12: Fe-SMA material behavior LP8 (0.03 %/sec up to 2 % strain amplitude and 0.8 %/sec after)

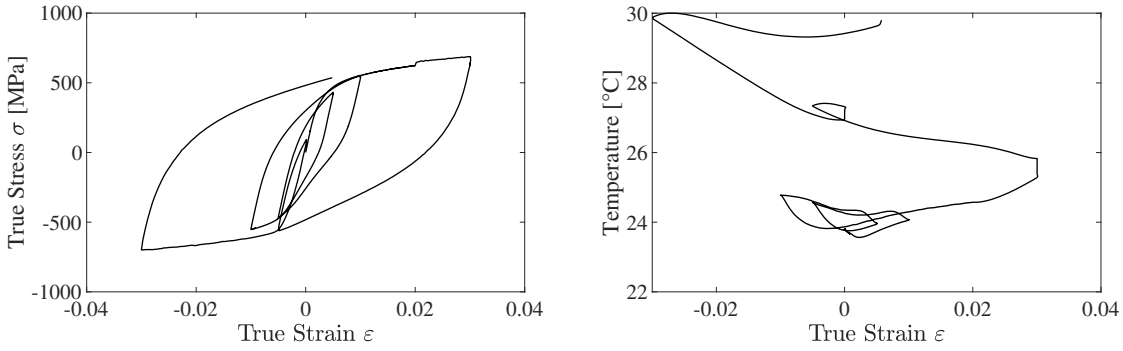

(a) True stress-true strain (b) Temperature-true strain

Figure 13: Fe-SMA material behavior LP9 (0.03 %/sec up to 2 % strain amplitude and 0.8 %/sec after)

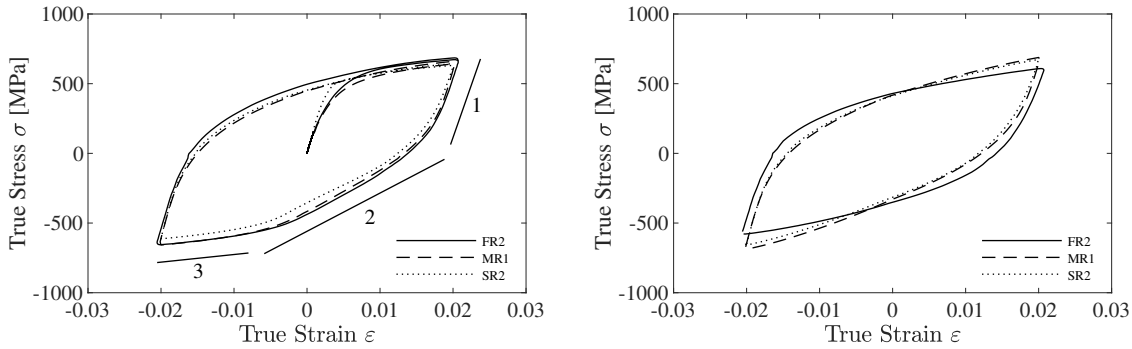

(a) First cycle (b) Last cycle (50^{th} cycle)

Figure 14: Comparison of the Fe-17Mn-5Si-10Cr-4Ni-1(V,C) (ma,-%) Fe-SMA true stress-true strain relationship for LP5 at different strain-rates

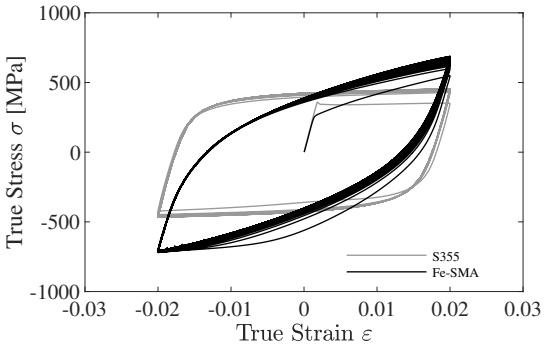

(a) S355J2+N and Fe-SMA

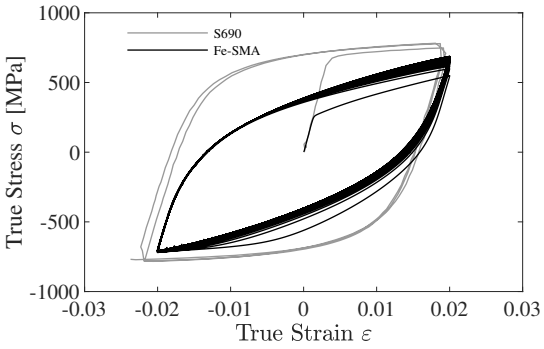

(b) S690QL and Fe-SMA

Figure 15: Comparison of the Fe-17Mn-5Si-10Cr-4Ni-1(V,C) (ma,-%) Fe-SMA and structural steels for LP5

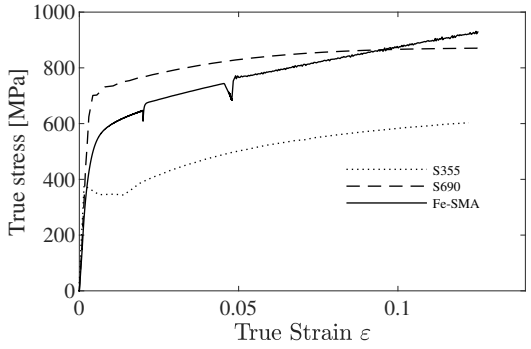

(a) True stress-true strain LP1

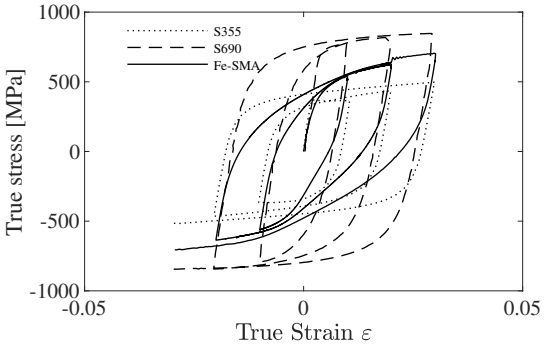

(b) True stress-true strain LP7

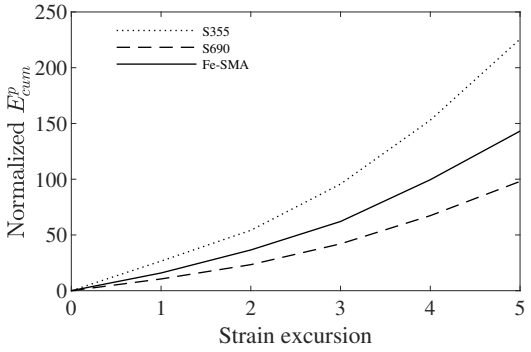

(c) Normalized energy dissipated LP7

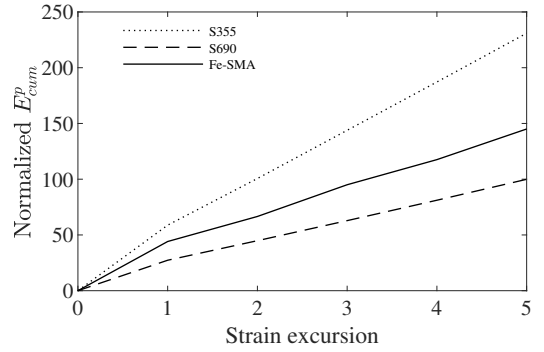

(d) Normalized energy dissipated LP5

Figure 16: Stress-strain and energy dissipation of the Fe-17Mn-5Si-10Cr-4Ni-1(V,C) (ma,-%) Fe-SMA and structural steels for LP1 and LP7